Thermal stress and probability of failure analyses of functionally graded solid oxide fuel cells

Ganesh Anandakumar [a], Na Li [b], Atul Verma [c], Prabhakar Singh [c], Jeong-Ho Kim [a],*

[a] Department of Civil and Environmental Engineering, University of Connecticut, 261 Glenbrook Rd, U-2037, Storrs, CT 06269, USA
[b] Department of Mechanical Engineering, University of Connecticut, USA
[c] Center for Clean Energy Engineering, University of Connecticut, USA

ABSTRACT

Thermal stresses and probability of failure of a functionally graded solid oxide fuel cell (SOFC) are investigated using graded finite elements. Two types of anode-supported SOFCs with different cathode materials are considered: NiO-YSZ/YSZ/LSM and NiO-YSZ/YSZ/GDC-LSCF. Thermal stresses are significantly reduced in a functionally graded SOFC as compared with a conventional layered SOFC when they are subject to spatially uniform and non-uniform temperature loads. Stress discontinuities are observed across the interfaces between the electrodes and the electrolyte for the layered SOFC due to material discontinuity. The total probability of failure is also computed using the Weibull analysis. For the regions of graded electrodes, we considered the gradation of mechanical properties (such as Young's modulus, the Poisson's ratio, the thermal expansion coefficient) and Weibull parameters (such as the characteristic strength and the Weibull modulus). A functionally graded SOFC showed the least probability of failure based on the continuum mechanics approach used herein.

© 2010 Elsevier B.V. All rights reserved.

1. Introduction

A solid oxide fuel cell (SOFC) is an electrochemical device, which converts the chemical energy of hydrocarbon fuels into electrical power at elevated temperatures [1,2]. It has recently received increasing attention due to its high power density, fuel flexibility, and strong potential for generating electricity and heat for industry and auxiliary power in vehicles. In addition to high-temperature (HT) SOFCs, intermediate-temperature (IT) SOFCs have also gained considerable attraction. A reduced operating temperature allows low cost metallic interconnects [3], helps avoid material compatibility challenges pervasive at high temperatures [4], reduces sealing and thermal degradation problems [5], and eventually accelerates the commercialization of SOFC technology. The mechanical strength of SOFC components is one of the key issues for determining their performance and reliability under transient and steady-state thermal loading. Stresses in SOFC components can arise from manufacturing process (e.g. residual stresses); mismatch in thermal expansion coefficients (TEC) of cell components; spatial or temporal temperature variations; oxygen activity gradients; redox cycling, and external mechanical loading. The magnitude of stresses depend on material properties, operating conditions and geometry of the cell design [6]. Stresses caused by thermal gradi-

ents and TEC mismatch tend to increase with increasing in-plane dimensions. Further, SOFC stacks are usually clamped during operation in order to secure proper alignment and good contact between the cell components. This, together with the seals required around the edges of planar cells to separate the fuel and air compartments, can cause higher mechanical stresses transmitted to brittle elements in the stacks.

Selimovic et al. [6] studied steady state and transient thermal stresses caused by spatial and temporal temperature gradients and TEC mismatch. Nakajo et al. [7] studied mechanical issues in a standard SOFC repeat unit with an anode-supported cell during assembly, heat-up, current–voltage (IV) characterization, dynamic operation, load shutdown and cool-down phases using a thermo-electrochemical model. They also calculated the probability of failure of the cells using the Weibull method [8]. Laurencin et al. [9] developed a numerical tool to study the risk of cell failure due to residual stresses arising after the manufacturing process, at both operating temperature and after anode re-oxidation, and also due to the presence of material singularity like crack. Lin et al. [10] performed finite element analysis to predict thermal stress distribution in a planar SOFC stack at various stages using a temperature field obtained from an integrated thermo-electrochemical model [11]. Khaleel et al. [12] developed an electrochemisty module to supplement the capability of commercial finite element analysis package MARC to model SOFCs. Williford and Singh [13] developed a two-layered porous high performance cathode design as a means of exploring new microstructure and material options for SOFCs.
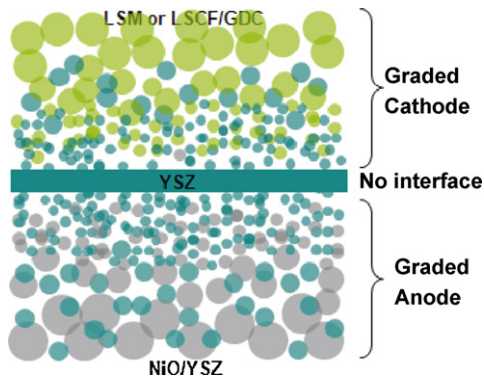
Fig. 1. Schematic of a unit cell SOFC with graded electrodes.

Fig. 2. Homogeneous vs. graded finite elements. (a) Property variation along the x-axis; (b) homogeneous elements; (c) graded elements. Note that the property of the homogeneous element corresponds to the property at its centroid [26].

For a traditional layered SOFC with Strontium-doped Lanthanum Manganite (LSM) as the cathode and Yttria Stabilized Zirconia (YSZ) as the electrolyte, the performance is often limited by the oxygen reduction processes at the cathode [14–16]. In order to improve the SOFC performance, material composition and microstructural skeleton must be optimized to provide a higher density of active sites such as triple phase boundaries. Towards this end, several composite electrodes such as YSZ-LSM, LSM-GDC (e.g. $Ce_{0.8}Gd_{0.2}O_2$, Gadolinium Doped Ceria), and GDC-LSCF (e.g. $(La,Sr)(Co,Fe)O_3$, Lanthanum Strontium Cobalt Ferrite) have been developed to improve electrode reactions and increase triple phase boundaries [17]. Grading both the anode and the cathode electrodes will enhance interlocking between the electrodes and the electrolyte and may improve electrochemical performance. Fig. 1 shows schematic of a SOFC with graded electrodes utilizing the concept of a functionally graded material (FGM). Graded regions in both electrode sides are realized by varying its composition, microstructure and porosity. As the composition changes, so do the effective material properties, thereby avoiding sharp material discontinuities which may otherwise result in delamination during thermal cycling [17]. Zha et al. [18] showed that graded cathodes fabricated using a sol–gel/slurry coating process led to relatively low polarization resistance at intermediate temperatures. Ni et al. [19] found that grading both porosity and particle size in the electrodes are effective to enhancing SOFC performance. Holtappels and Bagger [20] showed that five and nine layer cathodes have better electrochemical performance than a conventional two layer cathode mainly because of gradation of the composition and microstructure. From a mechanical viewpoint, the use of FG electrodes would greatly improve bonding strength and compatibility between electrodes and electrolyte, reduce the magnitude of residual and thermal stresses, and may reduce the crack driving force [21–23].

During the operation of the solid oxide fuel cell, rapid start-up and shut-down may be necessary in portable and transportable applications which may lead to rapid temperature changes. Rapid temperature change leads to significant temperature differences between the surface and the mean body leading to a state of thermal shock. A thermal shock introduces stress in a material due to temperature differences between the surface and the interior, or between different regions of the body [24]. When a body is subjected to an external disturbance thermally by sudden contact or very rapid body heating, the dynamic effect then depends on the ratio of two significant times: the thermal time (t_T) over which significant change in the external disturbance takes place i.e. the time measuring the rapidity of temperature rise in the body, and the mechanical time (t_M) characterizing the wave propagation across the body. Inertia plays a significant role in thermoelasticity if the thermal time is of the same order as that of the mechanical time
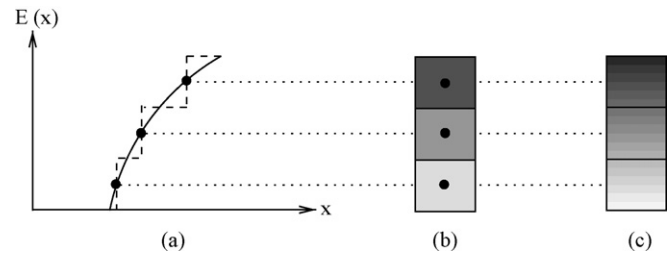
[25]. The transient nature of the temperature field in SOFC is partly due to the electrochemical reactions occurring in it. Although the temperature field in the SOFC is dynamic in nature when it goes through heat-up, steady state and shut-down phases, we can see that inertia does not play a significant role in the transient thermal stress analysis in the viewpoint of its temporal variation. As compared to high thermal gradients, a spatially uniform thermal loading can also create a state of thermal shock [25] in a body but the thermal time (t_T) has to be of the same order as that of the mechanical time (t_M). For the model considered in this paper, the mechanical time ($=L/c$, where L is the largest distance from the point where the external disturbance (thermal shock) occurs and c is the velocity of wave propagation) is of the order of few microseconds or lesser. This specific thermal shock problem is not quite relevant to SOFC applications.

The objective of this paper is to perform thermal stress and probability of failure analyses of functionally graded SOFC under spatially uniform and non-uniform temperature loads. We have not considered inertia effects and residual stresses the latter of which are specific to various steps of manufacturing processes and cell dimensions and configurations. All of the materials are assumed to behave as linear elastic and isotropic. Although SOFC electrodes are porous in reality, we modeled them as contiua with effective thermo-mechanical properties. We analyzed three-dimensional (3D) SOFCs consisting of NiO-YSZ/YSZ/LSM (LSM, $La_{0.8}Sr_{0.2}MnO_3$) and NiO-YSZ/YSZ/GDC-LSCF (GDC, $Ce_{0.8}Gd_{0.2}O_2$; LSCF, $La_{0.58}Sr_{0.4}Co_{0.2}Fe_{0.8}O_{3-\delta}$). We also studied a semi-functionally graded HT-SOFC which has functional layers placed between the electrodes and the electrolyte. The total probability of failure of the SOFC cell layers are computed using the Weibull analysis [8].

This paper is organized as follows. Section 2 presents 3D graded finite element formulation. Section 3 presents thermal stress analysis of layered, semi-FG, and FG SOFCs under spatially uniform and non-uniform thermal loads. Section 4 presents the probability of failure analysis of the SOFC using the Weibull analysis. Section 5 addresses conclusion and potential extension of the current work.

2. Three-dimensional graded finite elements

In this study, we used the displacement-based finite element method and graded finite elements [26] to model spatial material gradation using the direct Gaussian integration formulation. Fig. 2 shows graded finite elements compared with the conventional homogeneous finite elements. By means of the principle of virtual work, the element stiffness matrix ($\mathbf{k}^e$) and the equivalent nodal force vector ($\mathbf{f}^{ext}$) (under an initial strain (ε_0)) of a finite element are formulated as:

$$\mathbf{k}^e = \int_\Omega \mathbf{B}^T \mathbf{D}(\mathbf{x})\mathbf{B}d\Omega, \quad \mathbf{f}^{ext} = \int_\Omega \mathbf{B}^T \mathbf{D}(\mathbf{x})\varepsilon_0\,d\Omega \qquad (1)$$
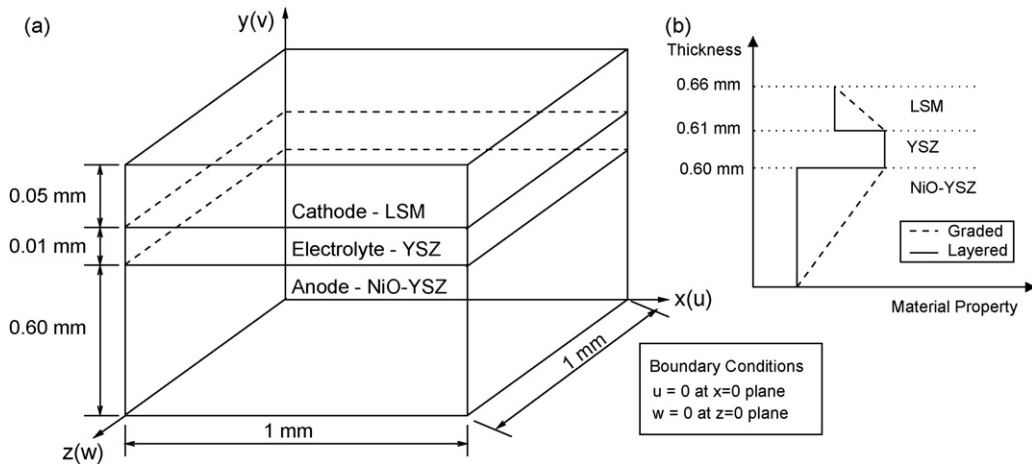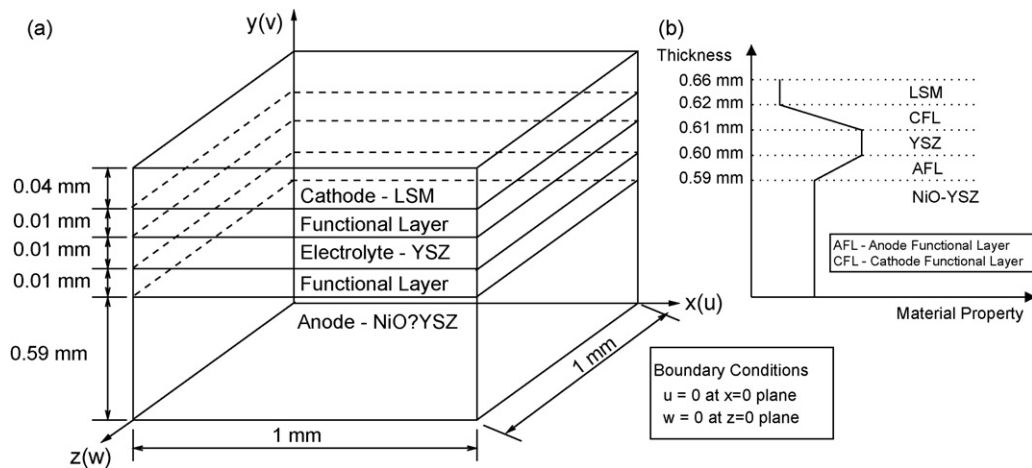
Fig. 3. A schematic of HT-SOFC.

Fig. 4. A schematic of semi-FG HT-SOFC.

where superscript T stands for transpose, $\mathbf{B}$ is shape function derivative matrix, $\mathbf{N}$ is shape function matrix, $\mathbf{D}(\mathbf{x})$ is constitutive matrix relating stresses to strains, $\varepsilon_0 = \alpha(\mathbf{x})\Delta T$, ΔT is the temperature difference between current state and stress free state, $\alpha(\mathbf{x})$ is the co-efficient of thermal expansion obtained at the Gauss points. The integral for the stiffness matrix and the equivalent thermal load vector are evaluated using Gaussian quadrature, and the matrix $\mathbf{D}(\mathbf{x})$ can be directly obtained by employing the Young's modulus and the Poisson's ratio at each Gaussian integration point. The resulting element stiffness matrix and the thermal load vector, for
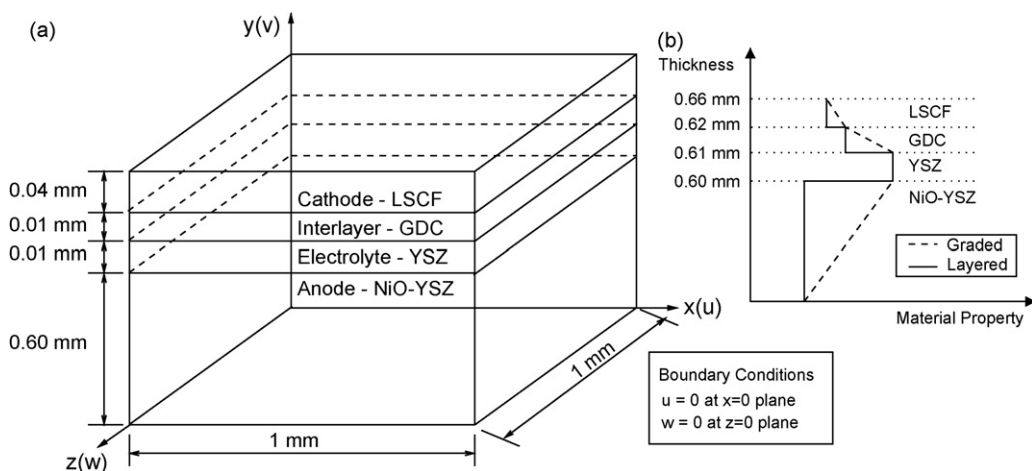

Fig. 5. A schematic of IT-SOFC.

Table 1
Material properties of fuel cell materials.

Cell layer	Thickness (μm)	Young's modulus (GPa)	Poisson's ratio	Density (kg m^{-3})	Thermal expansion coefficient (10^{-6} $^\circ$C^{-1})
NiO-YSZ	600	82 [43]	0.2 [44]	4200 [45]	13.2 [6]
YSZ	10	205 [43]	0.3 [46]	6010 [45]	10.4 [46]
LSM	50	40 [43]	0.25[46]	6350 [45]	11.4 [46]
GDC	10	155 [a]	0.3 [b]	7310 [28]	10 [c] [28]
LSCF	40	155 [a]	0.3 [b]	6350 [28]	11 [c] [28]

[a] The 98.5% relative density is considered for LSCF-GDC.
[b] Assumed.
[c] Room temperature TEC.

3D problems, become

$$\mathbf{k}^e = \sum_{i=1}^{n}\sum_{j=1}^{n}\sum_{k=1}^{n}\mathbf{B}^T\mathbf{D}(\Psi)\mathbf{B}Jw_iw_jw_k, \tag{2}$$

$$\mathbf{f}^{ext} = \sum_{i=1}^{n}\sum_{j=1}^{n}\sum_{k=1}^{n}\mathbf{B}^T\mathbf{D}(\Psi)\varepsilon_0Jw_iw_jw_k \tag{3}$$

where i, j, and k indicate the Gauss sampling points in the 3D finite element, $\Psi = \left(\xi, \eta, \zeta\right)$ are the Gauss point locations in the global domain, J is the determinant of the Jacobian matrix ($\mathbf{J}$), i.e., $J = \det(\mathbf{J})$ and w_i, w_j, and w_k are the weights of the sampling points. The thermal stress analysis is performed by solving the following linear equation:

$$\mathbf{K}\mathbf{u} = F_{ext} \tag{4}$$

where $\mathbf{K}$ and F_{ext} are the stiffness matrix and the external load vector of the finite element (FE) system, respectively, obtained after applying the boundary conditions, and $\mathbf{u}$ is the nodal degrees of freedom (DOF). Elastic strains (stresses) can be obtained from the displacement using a standard procedure (see for example [27]).

3. Thermal stress analysis of SOFCs

Figs. 3–5 show schematic of SOFC unit cell with boundary conditions and material properties variation, respectively for HT-SOFC, semi-FG HT-SOFC, and IT-SOFC. A quarter symmetric model with dimensions (1 mm × 0.66 mm × 1 mm) is used. Linear variation in material properties is assumed for anodes and cathodes such as NiO-YSZ, LSM (La$_{0.8}$Sr$_{0.2}$MnO$_3$), GDC (Ce$_{0.8}$Gd$_{0.2}$O$_2$), and LSCF (La$_{0.58}$Sr$_{0.4}$Co$_{0.2}$Fe$_{0.8}$O$_{3-\delta}$) whereas constant homogeneous material properties are used for YSZ. For the semi-FG HT-SOFC, a functional layer of thickness 10 μm is placed between the electrodes (NiO-YSZ and LSM) and the electrolyte (YSZ). Table 1 shows

material properties of fuel cell materials used for the present thermal analysis. Some are obtained from the literature and mechanical properties of the LSCF-GDC cathode are characterized in our present experiments (see Section 3.2.1 for more detail) [28].

We performed thermal stress analysis of SOFCs using the commercial finite element software ABAQUS [29]. Material variation within a finite element is obtained by implementing a user-defined subroutine (UMAT). Finite element results using ABAQUS agreed well with those obtained by our in-house finite element code, which are not provided in this paper. Following are Sections 3.1 and 3.2 which present thermal stress analysis results for anode-supported HT and IT SOFCs, respectively.
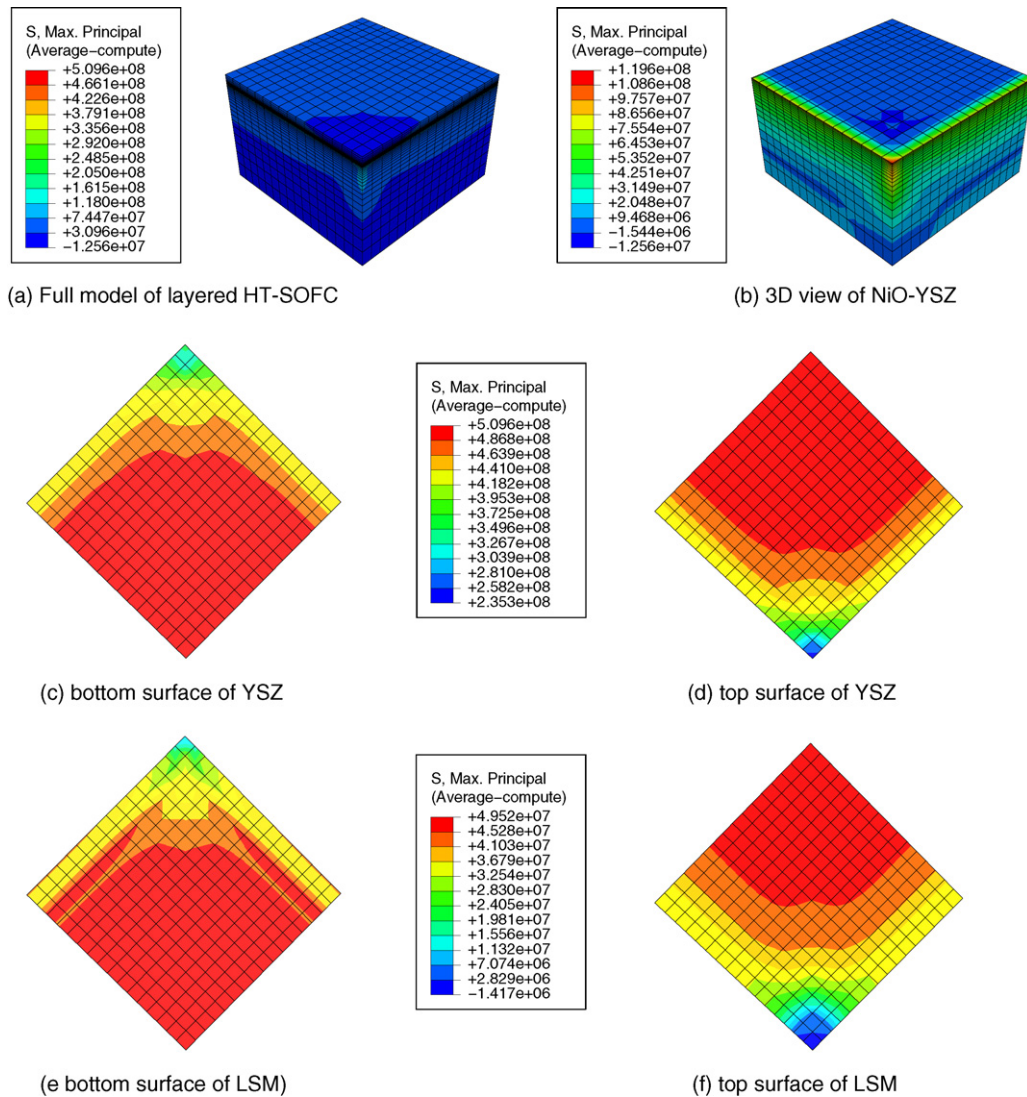
3.1. High-temperature SOFC: NiO-YSZ/YSZ/LSM

Fig. 6(a) shows the 3D finite element (FE) mesh of the quarter model (1 mm × 0.66 mm × 1 mm) of the SOFC unit cell. The FE mesh consists of 8704 8-node linear brick elements and 10,115 nodes for FG and layered HT-SOFC unit cell, and 8960 8-node linear brick elements and 10,404 nodes for semi-FG HT-SOFC unit cell. As shown in Fig. 6(b), finite elements are smaller through the thickness in size near the electrolyte–electrode interface to capture high stress grandients. A spatially uniform thermal loading is applied to the FE model of the unit cell along with symmetric displacement boundary conditions.

3.1.1. Functionally graded versus layered electrodes

Figs. 7 and 8 show contours of the maximum principal stress (MPS) in the layered and FG HT-SOFCs, respectively, under a uniform temperature loading of 800 $^\circ$C. As expected, the stress is symmetric about the diagonal due to the symmetric boundary conditions. The FG SOFC undergoes considerably lower stresses as compared to the layered SOFC. Considerable difference in the peak tensile MPS is seen in three layers of NIO-YSZ/YSZ/LSM in the

(a) (b)
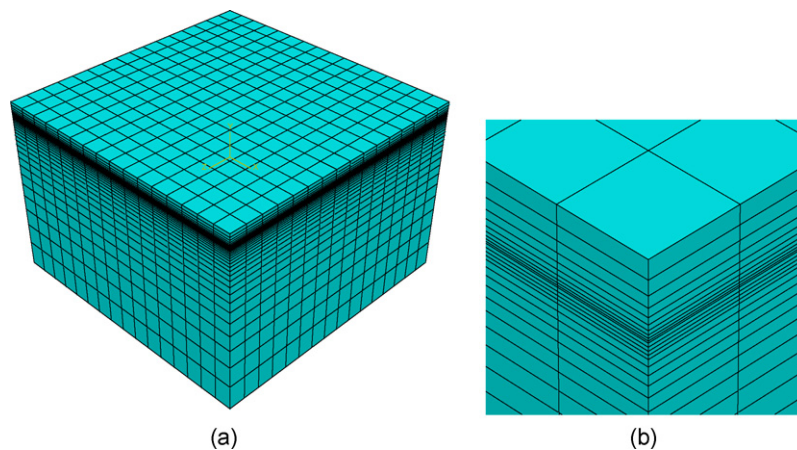
Fig. 6. The 3D finite element mesh consisting of 8704 8-node brick elements and 10,115 nodes in the (a) quarter symmetric model of a HT-SOFC unit cell and (b) close-up of the mesh at the top corner region.

(a) Full model of layered HT-SOFC

(b) 3D view of NiO-YSZ

(c) bottom surface of YSZ

(d) top surface of YSZ

(e bottom surface of LSM)

(f) top surface of LSM

Fig. 7. Maximum principal stress (Pa) contour of the layered HT-SOFC under spatially uniform temperature loading of $\Delta T = 800\,^{\circ}$C. Plots (a) and (b) show contours of the full SOFC model and NiO-YSZ layer, respectively. Plots (c) and (d), and (e) and (f) show contours of bottom and top surfaces of YSZ and LSM layers, respectively.

layered SOFC whereas the difference is negligible in the FG SOFC. Tensile stresses contribute significantly to crack initiation and growth in fuel cell ceramic layers although compressive stresses may lead to failure through delamination [30]. The peak compressive MPS in the layered SOFC is considerably lower compared to the peak tensile MPS. Stress discontinuities occur along the electrolyte–electrode interfaces in the layered SOFC due to material discontinuity. For the FG SOFC, the peak compressive MPS is comparable to the peak tensile MPS.

Comparing fracture strengths of individual fuel cell layers (see Table 2) with the MPS results, we see that the anode (NiO-YSZ) layer of the layered SOFC undergoes peak tensile stress (120 MPa) higher than its fracture strength (50–100 MPa). It occurs in a region close to the electrolyte interface (see Fig. 7(b)) which may indi-

cate interfacial cracking under the thermal loading considered herein. Considering the gradation of fracture strength from 50 to 100 MPa to 300 MPa, the anode layer (NiO-YSZ) of the FG SOFC undergoes the peak tensile MPS (52.7 MPa) near the electrolyte interface that is lower than the assumed graded fracture strength. The peak tensile MPS of the electrolyte (YSZ) layer (509 MPa) in the layered SOFC is also higher than its fracture strength of 300 MPa whereas it (49.8 MPa) is well below its fracture strength in the FG SOFC. The cathode layer of the layered SOFC undergoes the peak tensile MPS (49.5 MPa) that is lower than its fracture strength. The cathode (LSM) layer of the FG SOFC undergoes peak tensile MPS (56 MPa) near the electrolyte interface and is well below the fracture strength of 300 MPa at the electrolyte–electrode interface and comparable to 52 MPa at the outer boundary of the cathode.

3.1.2. Semi-functionally graded electrodes

Fig. 9 shows MPS contour of the semi-FG SOFC under a spatially uniform temperature loading of 800 °C. Tensile MPS is maximum in the anode functional layer (AFL) and least in the cathode (LSM) layer. We also see that the anode layer (NiO-YSZ) undergoes the peak tensile MPS (114 MPa) that is higher than its fracture strength. The peak tensile MPS of the anode functional layer (AFL) (513 MPa)

Table 2
Fracture strength of SOFC materials considered.

Cell layer	Fracture strength (MPa)
NiO-YSZ	50–100 [47]
YSZ	300 [48]
LSM	52 [49]
GDC	322 [24]
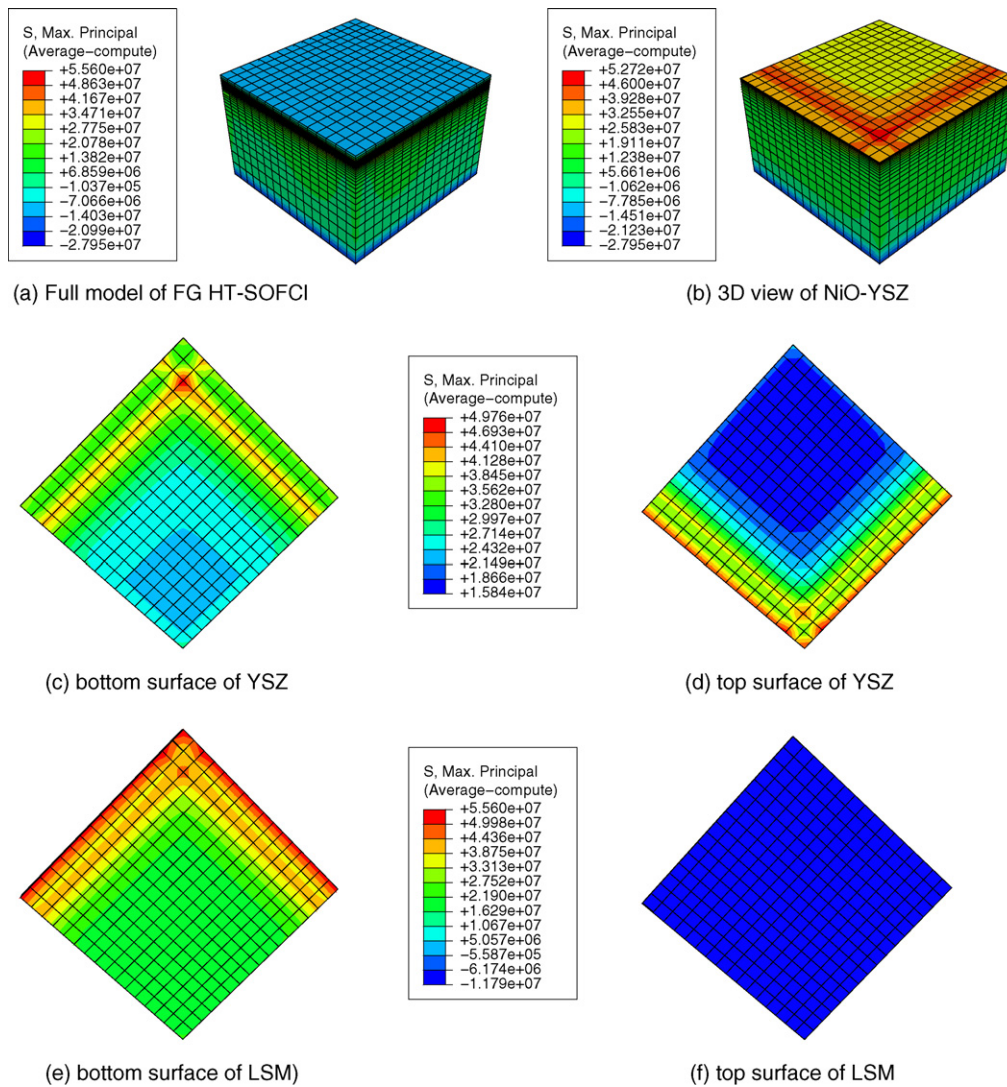
Fig. 8. Maximum principal stress (Pa) contour of the FG HT-SOFC under spatially uniform temperature loading of $\Delta T = 800\,^{\circ}$C. Plots (a) and (b) show contours of the full SOFC model and NiO-YSZ layer, respectively. Plots (c) and (d), and (e) and (f) show contours of bottom and top surfaces of YSZ and LSM layers, respectively.

occurs near the interface and is also higher than its fracture strength. Similarly, the peak tensile MPS of the cathode functional layer (CFL) (474.7 MPa) occurs near the interface and is also higher than its fracture strength. The peak tensile MPS (39.3 MPa) of the cathode layer (LSM), however, is lower than its fracture strength.

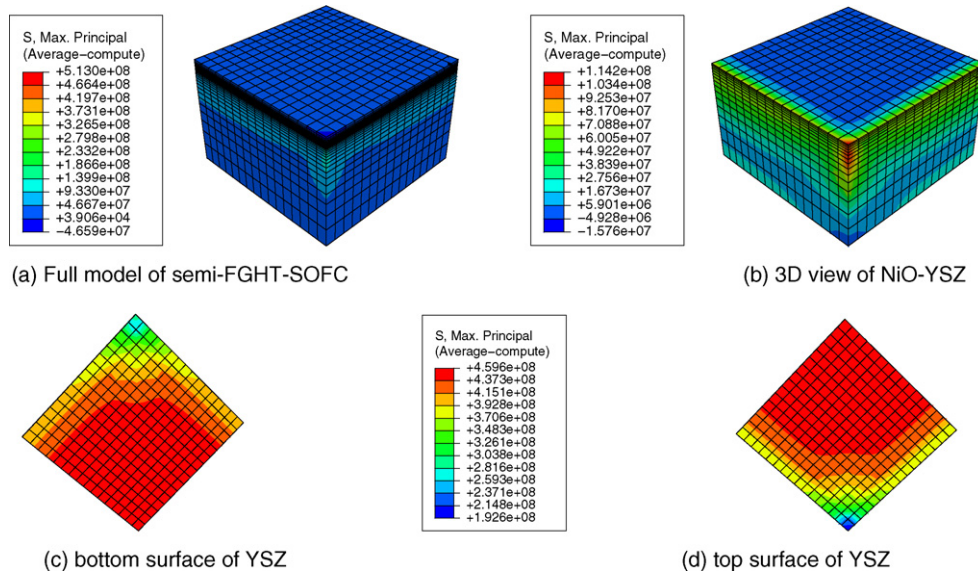### 3.2. Intermediate-temperature SOFC: NiO-YSZ/YSZ/GDC/LSCF

The material data for various volume fractions of LSCF-GDC available in the literature is not comprehensive for our present modeling. Thus we characterized material proparties such as Young's modulus and the thermal expansion coefficient of the LSCF-GDC cathode using state-of-the-art techniques, and using such properties, we performed a realistic finite element analysis for thermal stresses.

3.2.1. Material chacterization: LSCF-GDC

The LSCF (La$_{0.58}$Sr$_{0.4}$Co$_{0.2}$Fe$_{0.8}$O$_{3-\delta}$)-GDC (Ce$_{0.8}$Gd$_{0.2}$O$_2$) composite cathodes with different composition ratios were prepared for potential application for IT-SOFC with multifunctional graded cathodes. The LSCF La$_{0.58}$Sr$_{0.4}$Co$_{0.2}$Fe$_{0.8}$O$_x$ with a specific area 12.2 m^2 g^{-1} was purchased from SEIMI Chemical Cooperation, and the GDC Ce$_{0.8}$Gd$_{0.2}$O$_2$ with a specific area 11.4 m^2 g^{-1} was pur-

chased from DKKK in Japan. LSCF-GDC cathode powders were prepared by ball milling LSCF and GDC powders for 24 h in ethanol to achieve good mixing. Monolithic pellets and rectangular bars were obtained by dry pressing powders at about 200 MPa and then sintering at 1200° C respectively in air for 2 h with a heating rate 2 $^{\circ}$C/min. The linear shrinkage was calculated along the longitudinal dimension after sintering. The bulk density was determined by the Archimedes method. Theoretical density was calculated using the lattice parameters obtained from the diffraction analysis. The sintered bars were about $3 \times 4 \times 50$ mm in dimension. Pellets were about 10 mm in diameter and 2 mm in thickness. Rectangular samples were used for thermal expansion tests. Thermal expansion properties were measured using the NETZSCH 402PC dilatometer in air over a range from the room temperature to 1000° C with a heating rate 3 $^{\circ}$C/min. Standard alumina rod was used for calibration. The average thermal expansion coefficient (α) was calculated from the expansion. Nano indentation test was done using the MTS Nano Indenter XP. All pellets were tested at room temperature with 50 g applied load held for 30 s. All the data were recalculated using frame stiffness 3.9E+6. Young's modulus was calculated as follows:

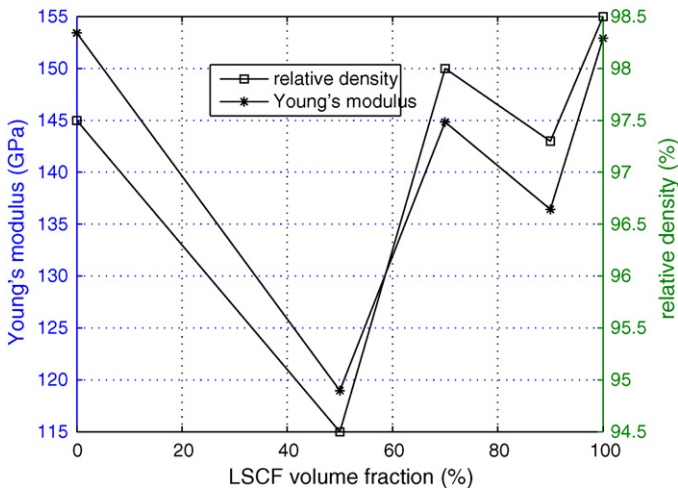$$\frac{1}{E_r} = \frac{1 - \nu_{indentor}^2}{E_{indentor}} + \frac{1 - \nu_{sample}^2}{E_{sample}} \tag{5}$$

(a) Full model of semi-FGHT-SOFC

(b) 3D view of NiO-YSZ

(c) bottom surface of YSZ

(d) top surface of YSZ

Fig. 9. Maximum principal stress (Pa) contour of the semi-FG HT-SOFC under spatially uniform temperature loading of $\Delta T = 800\,°C$. Plots (a) and (b) show contours of full SOFC model and NiO-YSZ layer, respectively. Plots (c) and (d) show bottom and top surfaces of the YSZ layer, respectively.

where $\nu_{indentor}$ and ν_{sample} are the Poisson's ratios of the indentor and the sample, respectively and $E_{indenter}$ and E_{sample} are the Young's modulus of the diamond indenter and the sample, respectively [31]. The Young's modulus of the sample was calculated using $\nu_{indenter}$ =0.07 and $E_{indenter}$ = 1140 Pa for the diamond indenter and assuming ν_{sample} =0.3 [32].

Fig. 10 shows the characterized Young's modulus and the relative density data. The relative density has a trend similar to the modulus change with LSCF contents. Young's modulus is insensitive to flaw size and is a measure of bonding at an atomic level, but porosity lowers the Young's modulus of ceramic materials. The modulus and density results of boron suboxide are successfully fitted using linear or power law [33]. We observe that the elastic modulus significantly depends on the density. Samples of 100% LSCF and 100% GDC in this experiment showed similar modulus values and we use identical Young's modulus values (155 GPa) for finite element modeling considering constant 98% relative density in the entire graded cathode region. The variation of the modulus is mainly due to the density rather than LSCF volume fraction.

All the samples sintered at $1200°$ C for 2 h were measured for the thermal expansion coefficient. They are comparable to the literature [34–39]. Fig. 11 shows the linear thermal expansion of LSCF-GDC composite cathode with 0, 50, 70, 90, and 100 wt% LSCF as a function of temperature. As expected, the percentage thermal expansion increases with temperature for all the samples. Among these three samples, the expansion is found to be the lowest for the GDC electrolyte. The doped samples had closer thermal expansion properties to one another than pure LSCF and GDC samples.

3.2.2. Finite element analysis

The 3D finite element (FE) mesh of the quarter model contains 8192 8-node linear brick elements and 9537 nodes which is similar to the mesh shown in Fig. 6. In this example, we considered both spatially uniform and non-uniform thermal loadings.

Following are finite element results for the uniform temperature fields in the SOFC unit cell. Figs. 12 and 13 show MPS contours of the layered and FG SOFCs, respectively, under a spatially uniform temperature loading of 600 °C. The FG SOFC undergoes considerably lower stresses as compared to the layered SOFC. Peak tensile MPS (104 MPa) for the anode (NiO-YSZ) layer in the layered SOFC is higher than its fracture strength (50–100 MPa). The electrolyte
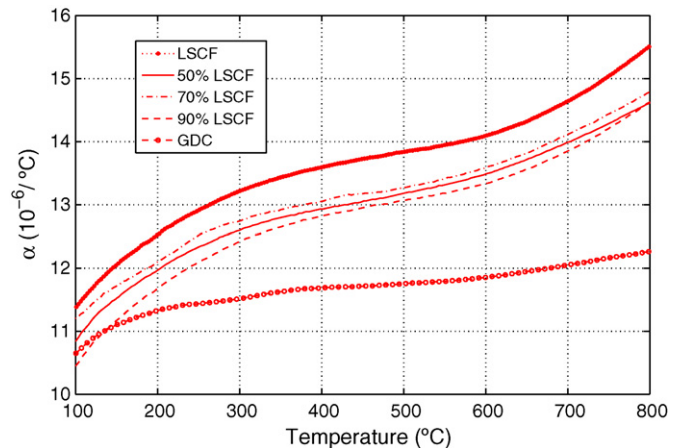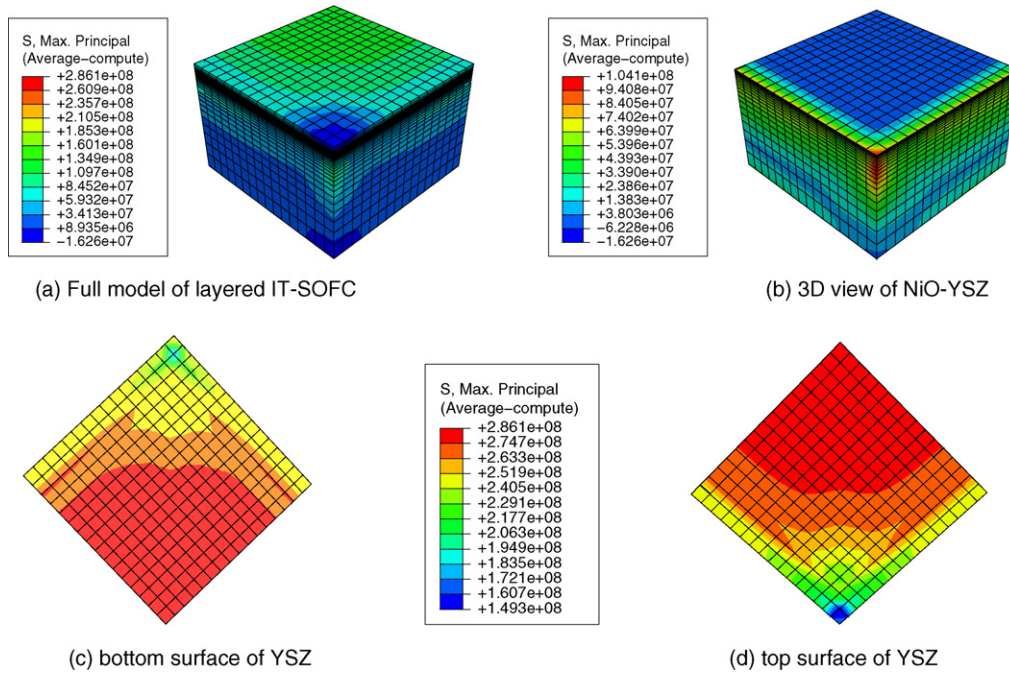

Fig. 10. Elastic modulus (measured by nano indentation) and the relative density (measured by the Archimedes method) for composite cathode samples with various LSCF volume fractions.

**Fig. 11.** Temperature-dependent thermal expansion coefficients (TECs) of LSCF/GDC composite measured in air.

Fig. 12. Maximum principal stress (Pa) contour of the layered IT-SOFC under spatially uniform temperature loading of $\Delta T = 600\,°C$. Plots (a) and (b) show contours of full SOFC model and NiO-YSZ layer, respectively. Plots (c) and (d) show bottom and top surfaces of the YSZ layer, respectively.

(YSZ) layer (286 MPa) and the GDC interlayer (265 MPa) undergo peak tensile MPS within the range of their fracture strengths of 300 MPa and 322 MPa, respectively. Since the fracture strength of LSCF is not found in the literature, no comparison is made for the peak tensile MPS in LSCF. The peak tensile MPS in the FG SOFC are well below its fracture strengths.

High temperature gradients occur in the SOFC layers during steady state and transient operation (heat-up, start-up, and shutdown) [6] and due to the grading of the porous electrode matrix and due to non-uniform Joule heating [40]. So far, we have studied the thermal stress behavior of the unit cell subjected to a spatially uniform temperature difference loading. In this section, we subject the unit cell SOFC to a linear temperature difference loading and study the stress behavior of layered and FG SOFC. The temperature difference loading is varied from $550\,°$ C at the left end ($x = 0$ mm) to $600\,°$ C at the right end ($x = 1$ mm). Same displacement boundary conditions are applied to the model as before. This type of temperature gradient may simulate some extreme thermal gradients in the cell (e.g. $50\,°C/mm$). Fig. 14 show MPS contours of the FG SOFCs under this spatially non-uniform (linearly varying) temperature loading.
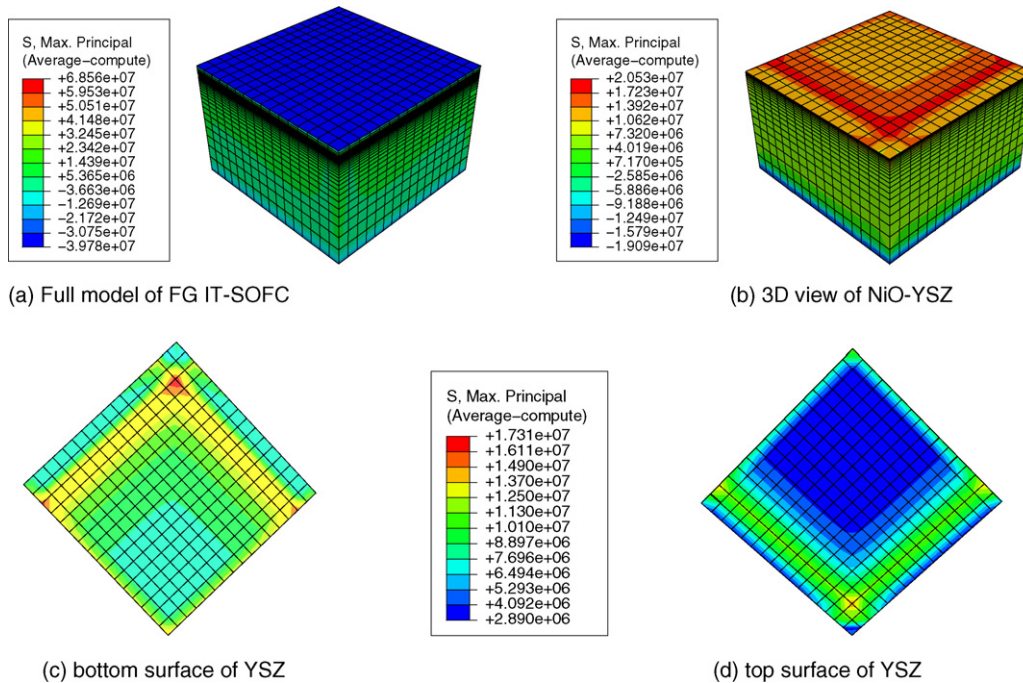
Fig. 13. Maximum principal stress (Pa) contour of the FG IT-SOFC under spatially uniform temperature loading of $\Delta T = 600\,°C$. Plots (a) and (b) show contours of full SOFC model and NiO-YSZ layer, respectively. Plots (c) and (d) show bottom and top surfaces of the YSZ layer, respectively.
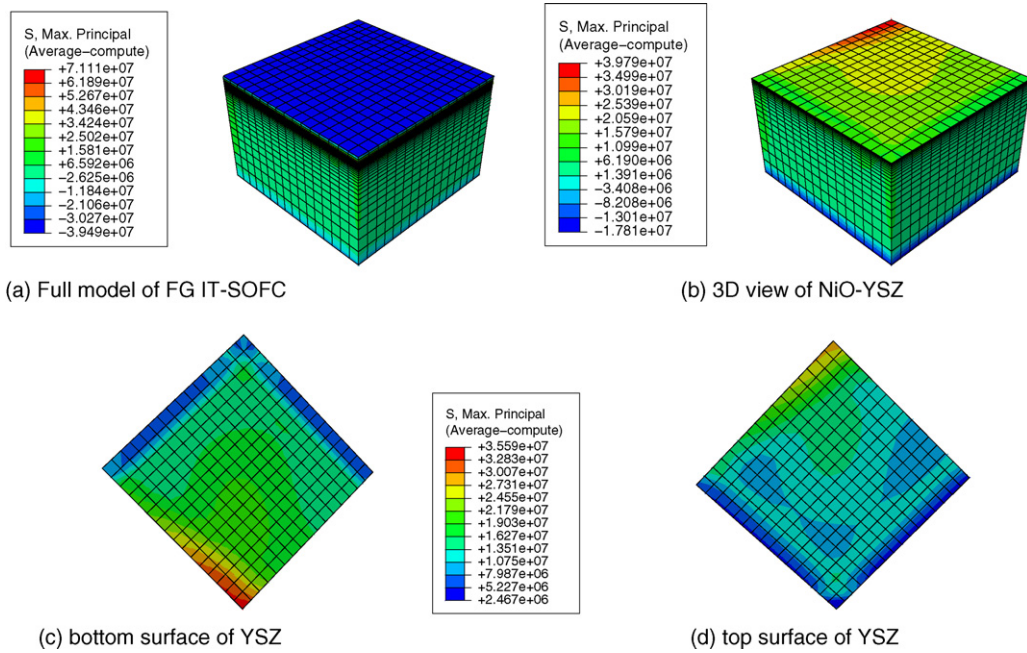
Fig. 14. Maximum principal stress (Pa) contour of the FG IT-SOFC under *linearly varying* temperature loading. Plots (a) and (b) show contours of full SOFC model and NiO-YSZ layer, respectively. Plots (c) and (d) show bottom and top surfaces of the YSZ layer, respectively.

The results for the layered IT-SOFC is not provided due to page limit. The FG SOFC undergoes lower MPS (tensile) than that for the layered SOFC. The stress is not symmetric due to the non-symmetric non-uniform temperature variation. Comparing fracture strengths with the peak tensile MPS in the cell, we see that the anode layer of the layered SOFC undergoes higher peak tensile MPS than its fracture strength. The YSZ electrolyte and the GDC interlayer of the layered SOFC undergo peak tensile MPS values close to their fracture strengths. The fuel cell layers in the FG SOFC undergo peak tensile MPS values much lower than their fracture strengths.

The advantage of having smooth material gradation at interfaces is to avoid stress discontinuity which usually leads to fracture and damage. We observed that stress discontinuity occurred for the layered SOFCs across the electrode–electrolyte interfaces. Fig. 15(a) and (b) shows the variation of MPS along the vertical thickness in HT- and IT-SOFCs, respectively, subject to a spatially uniform ther-

mal loading of 800 °C and 600 °C, respectively. The location selected for the stress output is near the region $x = 1$ mm and $z = 1$ mm of the FE model. We see that there is a huge stress jump for the layered SOFC at the interfaces because of the material discontinuity; however, for the graded SOFCs, the stress varies smoothly acorss the of the unit cell thereby leading to no stress discontinuities.

4. Probability of failure analysis

Ceramics including porous ceramics behave as brittle materials and exhibit a statistical strength distribution [9]. Thus the deterministic stress analysis for cermet materials as addressed so far may not lead to accurate and reliable physical interpretation. To this regard, the Weibull method [8] is utilized to estimate the risk of rupture and fracture. The method allows us to calculate the survival probability P_s of a structural component loaded with an applied
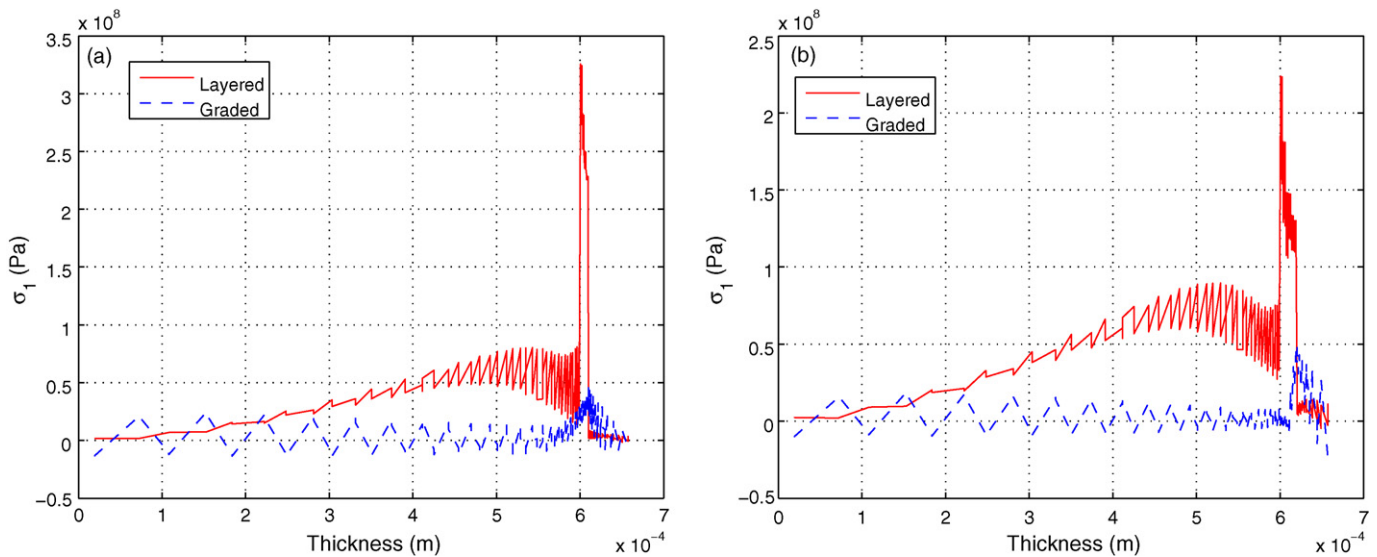
Fig. 15. The maximum principal stress (σ_1) along the thickness for (a) HT-SOFC (see Fig. 3) and (b) IT-SOFC (see Fig. 5) SOFCs considering layered (solid) and FG (dashed) material properties. Spatially uniform temperature loadings of 800 °C (HT-SOFC) and 600 °C (IT-SOFC) are applied.

Table 3
Weibull parameters of SOFC materials considered.

Cell layer	Weibull modulus, m	Characteristic strength, σ_0	Reference volume, V_0 (mm^3)
NiO-YSZ [50,49]	11.8	187.0	0.578
YSZ [51]	7.0	446.0	0.350
LSM [50,49]	7.0	52.0	1.21
GDC [52]	4.1	144.0	1.00 [a]
LSCF [b]	4.1	144.0	1.00

[a] Assumed equal to 1.0 mm^3.
[b] Assumed equal to GDC values.

tensile stress σ:

$$P_s^j(\sigma, V_j) = \exp\left(-\int_{V_j}\left(\frac{\sigma}{\sigma_0}\right)^m \frac{dV_j}{V_0}\right) \qquad (6)$$

with j = anode, electrolyte or cathode layer of the SOFC and V_j represents the volume of the jth layer. The characteristic strength σ_0 represents a scale parameter for the distribution whereas the Weibull modulus m corresponds to a shape parameter. The term V_0 is a reference volume linked to the characteristic strength. Table 3 lists the Weibull parameters of the cell layers which are obtained from the literature or assumed otherwise. The SOFC cell structure is usually subjected to a multi-axial stress state. Hence, the total survival probability can be calculated as a product of each survival probability determined for the three principal stresses σ_i as [9]:

$$P_s^j(\bar{\sigma}, V_j) = \prod_{i=1}^{3} P_s^j(\sigma_i, V_j) \quad \text{with} \quad P_s^j(\sigma_i, V_j) = \exp\left(-\int_{V_j}\left(\frac{\sigma_i}{\sigma_o}\right)^m \frac{dV_j}{V_0}\right) \qquad (7)$$

Total probability of failure (TPOF, P_f) can be calculated using the equation $P_f = 1.0 - P_s^j(\bar{\sigma}, V_j)$. Only tensile principal stresses are used for calculating the probability of survival in Eq. (7) although compressive stresses may induce failure through other mechanisms such as delamination [30].

The probability of failure analysis is performed for the SOFC unit cell under various spatially uniform thermal loadings ($\Delta T = 100, 200, \ldots, 800\,°C$). The integrand in Eq. (7) is numerically integrated within the volume of the individual cell layers by summing up the product of the principal stress values $(\sigma_i)^m$ at the Gaussian integration points (multiplied by the determinant of the Jacobian and its Gauss weight) and the Weibull parameters $((1/\sigma_0)^m/V_0)$ listed in Table 3.

Fig. 16 shows a semi-log plot of the total probability of failure (TPOF) of the layered and FG HT-SOFC under various uniform thermal loadings. For the graded regions, the Weibull parameters such as the characteristic strength (σ_0) and the Weibull modulus (m) are linearly graded for NiO-YSZ and LSM layers. The reference volume V_0 is kept a constant. We see that the TPOF in layers of the FG SOFC is considerably lower as compared to the layered and semi-FG SOFCs.
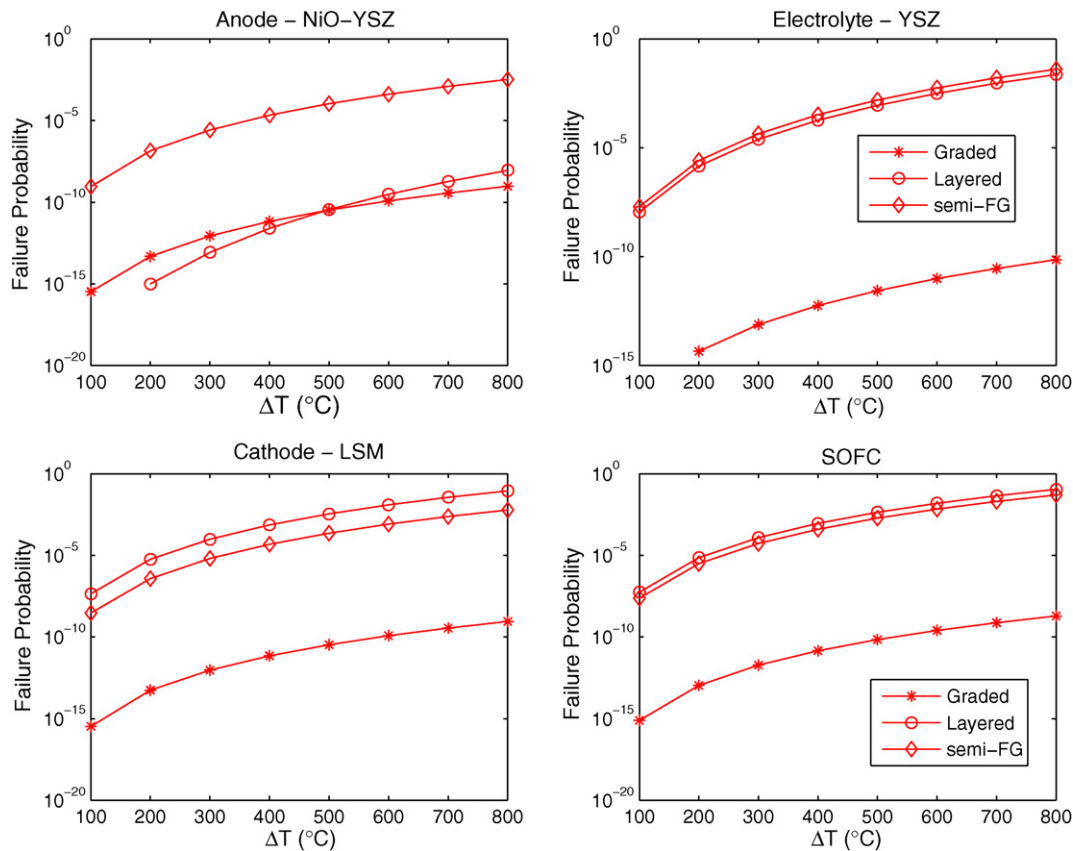
Fig. 16. Comparison of the total probability of failure of HT-SOFC considering layered (○) and graded (*) material properties and semi-FG (◊) HT-SOFC, which are subject to uniform temperature loads.
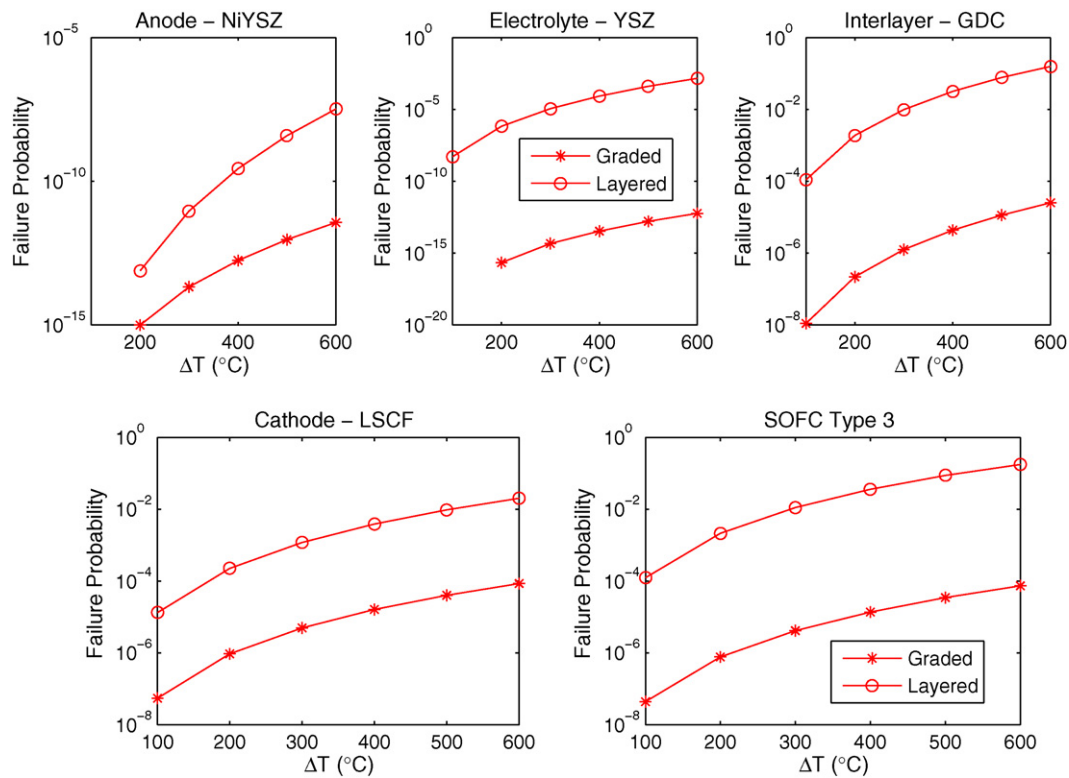
Fig. 17. Comparison of the total probability of failure of IT-SOFC considering layered (○) and graded (*) material properties whichis subject to uniform temperature loads.

Table 4
Total probability of failure for IT-SOFC under constant and linearly varying temperature variation.

ΔT	Model	Full model	NiO-YSZ	YSZ	GDC	LSCF
Linear	Layered	8.67E−02	1.33E−11	5.91E−02	2.93E−02	1.09E−06
	Graded	1.58E−04	6.25E−06	1.04E−05	8.84E−06	1.33E−04
Constant	Layered	1.76E−01	3.30E−08	1.47E−03	1.57E−01	2.02E−02
	Graded	7.35E−05	3.68E−12	5.88E−13	2.52E−05	8.50E−05

For the anode layer, the FG SOFC undergoes slightly higher TPOF for temperature loads up to 500 °C. For practical applications, it has been pointed out that the failure probability of SOFCs should be less than 1E-05 [41] or even 1E-06 [41,42]. For the FG SOFC, the failure probabilities are lower than these practical values for all the three layers.

For the layered HT-SOFC, we see that except for the anode layer, the electrolyte and the cathode layers undergo much higher TPOF values than these practical limits. In particular, the TPOF of the cathode of the layered SOFC is about 0.09 for the thermal loading of 800 ° C which is significantly higher than the practical limits. We also see that the TPOF for the full FG SOFC is significantly lower than that of the layered and the semi-FG SOFC.

Fig. 17 shows the semi-log plot of the TPOF of the IT-SOFC considering layered and FG material properties under various spatially uniform thermal loadings. We see that the TPOF of the cell layers of the FG unit cell SOFC is considerably lower as compared to the layered unit cell SOFC. The TPOF values of GDC and LSCF for the layered SOFC at the operating temperature loading of 600 ° C is about 0.15 and 0.02, respectively, which are significantly higher than the practical limits. The TPOF of GDC (2.5E−5) and LSCF (8.5E−5) for the FG SOFC at the operating temperature loading of 600 ° C is slightly higher than the practical limits. We also see that the TPOF for the full FG SOFC is significantly lower as compared to the layered SOFC.

Table 4 shows the total probability of failure obtained for the IT-SOFC considering layered and FG material properties under the linearly-varying temperature loading of 550 ° C at the left end

($x = 0$ mm) to 600 ° C at the right end ($x = 1$ mm). We see for constant and linear temperature loads that the TPOF is significantly lower for the graded SOFC as compared to the layered SOFC. For the given boundary and loading conditions considered, the TPOF of the layered IT-SOFC under the linear temperature load is less than that for the constant temperature load, and the opposite for the graded IT-SOFC.

5. Concluding remarks

Thermal stress and probability of failure analyses of SOFCs with functionally graded electrodes under spatially uniform and non-uniform temperature loads are performed using the finite element method. The novelties of this paper are the consideration of functionally graded electrodes in HT and IT SOFCs. The enhanced mechanical durability of FG SOFCs was observed over non-graded SOFCs. Material gradation modeled using graded finite elements is the main factor of this improvement. Two different material configurations of SOFCs are considered: NiO-YSZ/YSZ/LSM and NiO-YSZ/YSZ/GDC-LSCF. A user-defined subroutine (UMAT) is developed to discretize material properties which are graded in the SOFC unit cell. For the selected material sets, cell configurations, displacement and loading boundary conditions as well as no-residual-stress assumptions, functionally graded SOFCs experience considerably less thermal stresses and TPOF than those for the layered SOFC.

Assumptions and limitations of the present work are as follow. We assumed linear elasticity and isotropic material behavior. We also assumed spatially uniform and lineary-varying temperature fields. We have not considered inertia effects and residual stresses. The change of porosity and mechanical properties in the anode composite NiO-YSZ due to redox cycling is not considered. A potential and natural extension of the present work is to consider realistic temperature loads, include residual stresses, and use temperature-dependent properties for the finite element modeling, and perform multiscale modeling which addresses microstructure of porous electrodes in combination with flow, thermal, chemical and electrochemical phenomena.

Acknowledgements

References

[1] N.Q. Minh, T. Takahashi, Science and Technology of Ceramic Fuel Cells, Amsterdam, The Netherlands, 1995.
[2] S.C. Singhal, K. Kendall, High Temperature Solid Oxide Fuel Cells: Fundamentals, Design and Applications, Elsevier Ltd., 2003.
[3] S.P. Jiang, W. Wang, Journal of the Electrochemical Society 152 (7) (2005) A1398–A1408.
[4] Z. Duan, M. Yang, A. Yan, Z. Hou, Y. Dong, Y. Chong, M. Cheng, W. Yang, Journal of Power Sources 160 (2006) 57–64.
[5] E.P. Murray, M.J. Sever, S.A. Barnett, Solid State Ionics 148 (2002) 27–34.
[6] A. Selimovic, M. Kemm, T. Torisson, M. Assadi, Journal of Power Sources 145 (2005) 463–469.
[7] A. Nakajo, Z. Wuillemin, J.V. Herle, D. Favrat, Journal of Power Sources 193 (2009) 203–215.
[8] W. Weibull, Proceedings of the Royal Swedish Institute of Engineering Research 151 (1939) 1–45.
[9] J. Laurencin, G. Delette, F. L-Joud, M. Dupeux, Journal of the European Ceramic Society (2008) 1857–1869.
[10] C.K. Lin, T.T. Chen, Y.P. Chyou, L.K. Chiang, Journal of Power Sources 164 (2007) 238–251.
[11] Y-P. Chyou, T-D. Chung, J-S. Chen, R-F. Shie, Journal of Power Sources 139 (2005) 126–140.
[12] M.A. Khaleel, Z. Lin, P. Singh, W. Surdoval, D. Collin, Journal of Power Sources 130 (2004) 136–148.
[13] R.E. Williford, P. Singh, Journal of Power Sources 128 (1) (2004) 45–53.
[14] M.J.L. Ostergard, C. Clausen, C. Bagger, M. Mogensen, Electrochimica Acta 40 (1995) 1971–1981.
[15] J.V. Herle, A.J. McEvoy, K.R. Thampi, Electrochimica Acta 41 (1996) 1447–1454.
[16] C.W. Tanner, K.Z. Fung, A.V. Virkar, Journal of the European Ceramic Society 144 (1997) 21–30.
[17] N.T. Hart, N.P. Brandon, M.J. Day, J.E. Shemilt, Journal of Material Science 36 (2001) 1077–1085.
[18] S. Zha, Y. Zhang, M. Liu, Solid State Ionics 176 (2005) 25–31.
[19] M. Ni, M.K.H. Leung, D.Y.C. Leung, Journal of Power Sources 168 (2007) 369–378.
[20] P. Holtappels, C. Bagger, Journal of the European Ceramic Society 22 (2002) 41–48.
[21] F. Erdogan, B.H. Wu, Journal of Thermal Stresses 19 (3) (1996) 237–265.
[22] Y.-D. Lee, F. Erdogan, International Journal of Fracture 69 (2) (1995) 145–165.
[23] S. Suresh, A. Mortensen, Fundamentals of Functionally Graded Materials, IOM Communications Ltd., London, 1998.
[24] Y. Du, N.M. Sammes, G.A. Tompsett, D. Zhang, J. Swan, M. Bowden, Journal of the Electrochemical Society 150 (1) (2003) A74–A78.
[25] H.W. Bargmann, Journal of Thermal Stresses 15 (1992) 229–240.
[26] J.-H. Kim, G.H. Paulino, Journal of Applied Mechanics, Transactions ASME 69 (4) (2002) 502–514.
[27] R.D. Cook, D.S. Malkus, M.E. Plesha, R.J. Witt, Concepts and Applications of Finite Element Analysis, 4th edition, John Wiley & Sons, Inc., New York, 2001.
[28] N. Li, A. Smirnova, A. Verma, P. Singh, J.-H. Kim, Preparation and Characterization of LSCF (La$_{0.58}$Sr$_{0.4}$Co$_{0.2}$Fe$_{0.8}$O$_{3-\delta}$)/GDC (Ce$_{0.8}$Gd$_{0.2}$O$_2$) Cathode for IT-solid Oxide Fuel Cell, ACS, Florida, 2010.
[29] Hibbitt, Karlson & Sorensen, ABAQUS/Standard User's Manual, Hibbitt, Karlson & Sorensen, Inc., Pawtucket, RI, 2007.
[30] D. Sarantaridis, R.A. Rudkin, A. Atkinson, Journal of Power Sources 180 (2008) 704–710.
[31] Y. Wang, K. Duncan, E.D. Wachsman, F. Ebrahimi, Solid State Ionics 178 (1–2) (2007) 53–58.
[32] Y.S. Chou, J.W. Stevenson, T.R. Armstrong, L.R. Pedernson, Journal of the American Ceramic Society 83 (6) (2000) 1457–1464.
[33] D. Music, U. Kreissig, Zs. Czigny, U. Helmersson, J.M. Schneider, Applied Physics A: Materials Science & Processing 76 (2) (2003) 269–271.
[34] H. Hayashi, M. Kanoh, C.J. Quan, H. Inaba, S. Wang, M. Dokiya, H. Tagawa, Solid State Ionics 132 (3–4) (2000) 227–233.
[35] L.W. Tai, M.M. Nasrallah, H.U. Anderson, D.M. Sparlin, S.R. Sehlin, Solid State Ionics 76 (3–4) (1995) 273–283.
[36] S. Wang, M. Katsuki, M. Dokiya, T. Hashimoto, Solid State Ionics 159 (1–2) (2003) 71–78.
[37] A. Mineshige, J. Izutsu, M. Nakamura, K. Nigaki, J. Abe, M. Kobune, S. Fujii, T. Yazawa, Solid State Ionics 176 (11–12) (2005) 1145–1149.
[38] P. Zeng, R. Ran, Z. Chen, H. Gu, Z. Shao, J.C. Diniz da Costa, S. Liu, Journal of Membrane Science 302 (1–2) (2007) 171–179.
[39] P. Ried, P. Holtappels, A. Wichser, A. Ulrich, T. Graule, Journal of The Electrochemical Society 155 (10) (2008) B1029–B1035.
[40] I. Zinovik, D. Poulikakos, Electrochimica Acta 54 (26) (2009) 6234–6243.
[41] C.S. Montross, H. Yokokawa, M. Dokiya, British Ceramic Transactions 101 (9) (2002) 85–93.
[42] A. Nakajo, C. Stiller, G. Harkegard, O. Bolland, Journal of Power Sources 158 (2006) 294–387.
[43] S. Giraud, J. Canel, Journal of the European Ceramic Society 28 (2008) 77–83.
[44] A. Selcuk, A. Atkinson, Journal of the European Ceramic Society 17 (1997) 1523–1532.
[45] N. Srivastava, Modeling of solid oxide fuel cell/gas turbine hybrid systems, M.S. Thesis, The Florida State University, FL, 2006.
[46] S. Pitakthapanaphong, E.P. Busso, Modeling and Simulation in Materials Science and Engineering 13 (2005) 531–540.
[47] W. Fischer, J. Malzbender, G. Blass, R.W. Steinbrech, Journal of Power Sources 150 (2005) 73–77.
[48] N. Bamba, Y.H. Choa, K. Niihara, Nanostructured Materials 9 (1–8) (1997) 497–500.
[49] A. Atkinson, A. Selcuk, Solid State Ionics 134 (2000) 59–66.
[50] A. Atkinson, A. Selcuk, Proceedings of the 5th International Symposium on SOFC (SOFC V), Electrochemical Society, vols. 97–81, 1997, pp. 671–680.
[51] A. Selcuk, A. Atkinson, Journal of the American Ceramic Society 83 (8) (2000) 2029–2035.
[52] M. Trunec, Journal of the European Ceramic Society 24 (2004) 645–651.